LETTER

doi:10.1038/nature23656

Real-space imaging of non-collinear antiferromagnetic order with a single-spin magnetometer

I. Gross[1,2]*, W. Akhtar[1]*, V. Garcia[3], L. J. Martínez[1], S. Chouaieb[1], K. Garcia[3], C. Carrétéro[3], A. Barthélémy[3], P. Appel[4], P. Maletinsky[4], J.-V. Kim[5], J. Y. Chauleau[6,7], N. Jaouen[7], M. Viret[6], M. Bibes[3], S. Fusil[3,8] & V. Jacques[1]

Although ferromagnets have many applications, their large magnetization and the resulting energy cost for switching magnetic moments bring into question their suitability for reliable low-power spintronic devices. Non-collinear antiferromagnetic systems do not suffer from this problem, and often have extra functionalities: non-collinear spin order[1] may break space-inversion symmetry[2,3] and thus allow electric-field control of magnetism[4,5], or may produce emergent spin–orbit effects[6] that enable efficient spin–charge interconversion[7]. To harness these traits for next-generation spintronics, the nanoscale control and imaging capabilities that are now routine for ferromagnets must be developed for antiferromagnetic systems. Here, using a non-invasive, scanning single-spin magnetometer based on a nitrogen–vacancy defect in diamond[8–10], we demonstrate real-space visualization of non-collinear antiferromagnetic order in a magnetic thin film at room temperature. We image the spin cycloid of a multiferroic bismuth ferrite ($BiFeO_3$) thin film and extract a period of about 70 nanometres, consistent with values determined by macroscopic diffraction[11,12]. In addition, we take advantage of the magnetoelectric coupling present in $BiFeO_3$ to manipulate the cycloid propagation direction by an electric field. Besides highlighting the potential of nitrogen–vacancy magnetometry for imaging complex antiferromagnetic orders at the nanoscale, these results demonstrate how $BiFeO_3$ can be used in the design of reconfigurable nanoscale spin textures.

Nearly 90% of known magnetic materials have dominant antiferromagnetic interactions, resulting in no or very small magnetization, and most are also insulators[1]. This strongly impedes their investigation, especially when the magnetic order needs to be mapped at the nanoscale. Although magnetic force microscopy[13] or X-ray photoemission electron microscopy[14] can reach a spatial resolution of a few tens of nanometres, their sensitivities are not compatible with the detection of weak magnetic signals commonly involved in antiferromagnets. Spin-polarized scanning tunnelling microscopy can resolve the magnetic moments of single atoms[15] but is only applicable to conductive systems. Therefore, the spin texture of the vast majority of magnetically ordered materials cannot be directly imaged at the nanoscale. This is increasingly problematic because materials with complex antiferromagnetic orders show very appealing functionalities, which are absent in ferromagnets and are starting to be exploited in a new generation of low-power spintronic devices[16].

Typical examples are multiferroics, in which antiferromagnetism coexists with ferroelectricity, enabling an efficient electrical control of magnetization through magnetoelectric coupling[3–5]. Bismuth ferrite, $BiFeO_3$ (BFO), is such a multiferroic material[17], which is currently emerging as a unique platform for spintronic[5] and magnonic devices[18] because its multiferroic phase is preserved well above room temperature. However, whereas the ferroelectric properties of BFO have been widely investigated by piezoresponse force microscopy (PFM), revealing unique domain structures and domain wall functionalities[19,20], the corresponding nanoscale magnetic textures and their potential for spin-based technology still remain concealed. In this work we demonstrate real-space imaging and electric field manipulation of complex antiferromagnetic order in a BFO thin film by using an atomic-sized magnetometer based on a single nitrogen–vacancy (NV) defect in diamond.

Bulk BFO crystallizes in a slightly distorted rhombohedral structure, but is commonly described by the pseudocubic unit cell shown in Fig. 1a. The displacement of Bi ions relative to the FeO_6 octahedra gives rise to a strong ferroelectric polarization ($100\,\mu C\,cm^{-2}$) along one of the [111] directions[17]. This system is complex, as the eight possible polarization orientations $\boldsymbol{P}_i^{\pm}$ give rise to three types of ferroelectric domain walls (71°, 109° or 180°). From the magnetic point of view, BFO was initially thought to be a conventional G-type antiferromagnet[21] but high-resolution neutron diffraction later revealed a cycloidal antiferromagnetic order[11,12] with a characteristic wavelength of $\lambda \approx 64$ nm (Fig. 1b). The spin cycloid propagation direction and the ferroelectric polarization vector are normal to each other and are linked by magnetoelectric coupling. In addition, the rhombohedral symmetry of BFO allows three equivalent propagation directions of the cycloid ($\boldsymbol{k}_1$, $\boldsymbol{k}_2$, $\boldsymbol{k}_3$) for a given variant of ferroelectric domain[12,21] (Fig. 1c).

A 32-nm-thick BFO(001) film was grown by pulsed laser deposition on a $DyScO_3$(110) orthorhombic substrate, using an ultrathin buffer electrode of $SrRuO_3$ (see Methods and Extended Data Fig. 1). Epitaxial strain leads to an array of striped ferroelectric domains whose typical width is in the range of about 100 nm (Fig. 1d). In-depth PFM and X-ray diffraction analysis reveal that only two variants of polarization coexist ($\boldsymbol{P}_3^-$ and $\boldsymbol{P}_4^-$, see Fig. 1d), separated by 71° domain walls (Methods and Extended Data Figs 2 and 3). In thin films the spin cycloid can be modulated or even destroyed by epitaxial strain. Considering the low lattice mismatch between BFO and $DyScO_3$ (about 0.4%), the cycloidal antiferromagnetic order is however expected to be preserved in the studied epitaxial thin film[22].

The spin texture of the BFO sample was investigated through stray field measurements using a scanning nanomagnetometer based on a single NV defect in diamond[8–10]. This point-like impurity can be exploited for quantitative magnetic field imaging at the nanoscale by recording Zeeman shifts of its electronic spin sublevels through optical detection of the electron spin resonance (ESR). For the present study, a single NV defect placed at the apex of a nanopillar in a diamond scanning probe is integrated into an atomic force microscope, which allows the NV defect to be scanned in close proximity to a sample[23] (Fig. 2a). At each point of the scan, optical illumination combined with

[1]Laboratoire Charles Coulomb, Université de Montpellier and CNRS, 34095 Montpellier, France. [2]Laboratoire Aimé Cotton, CNRS, Université Paris-Sud, ENS Cachan, Université Paris-Saclay, 91405 Orsay, France. [3]Unité Mixte de Physique, CNRS, Thales, Université Paris-Sud, Université Paris-Saclay, 91767 Palaiseau, France. [4]Department of Physics, University of Basel, Klingelbergstrasse 82, Basel CH-4056, Switzerland. [5]Centre de Nanosciences et de Nanotechnologies, CNRS, Université Paris-Sud, Université Paris-Saclay, 91405 Orsay, France. [6]SPEC, CEA, CNRS, Université Paris-Saclay, 91191 Gif-sur-Yvette, France. [7]Synchrotron SOLEIL, 91192 Gif-sur-Yvette, France. [8]Université d'Evry, Université Paris-Saclay, 91025 Evry, France.
*These authors contributed equally to this work.

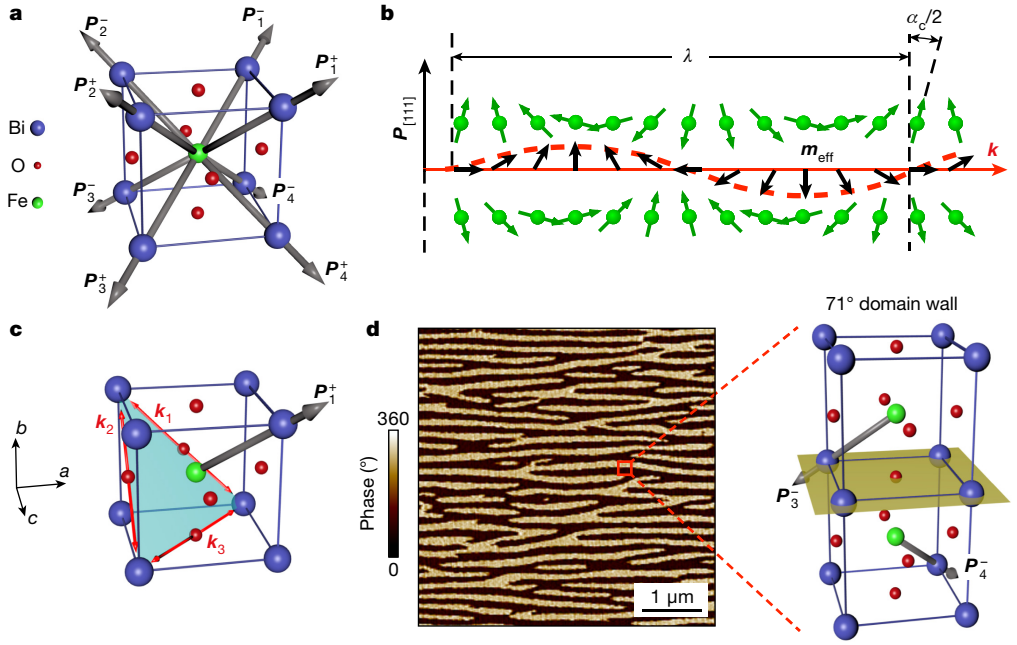

Figure 1 | Ferroelectric and magnetic order in $BiFeO_3$. a, Pseudocubic unit cell of $BiFeO_3$ (BFO) showing the possible variants of the ferroelectric polarization $\boldsymbol{P}_i^{\pm}$ pointing along the eight [111] directions. **b**, Schematic representation of the spin cycloid. Magnetoelectric coupling induces a cycloidal rotation of Fe^{3+} spins (green arrows). The canted antiferromagnetic alignment between consecutive atomic layers, characterized by the angle α_c, results in an effective magnetic moment $\boldsymbol{m}_{eff}$ describing a cycloid with wavelength λ (black arrows). The propagation direction of the spin cycloid $\boldsymbol{k}$ is normal to the ferroelectric polarization vector $\boldsymbol{P}$. **c**, Representation of a given variant of the ferroelectric polarization ($\boldsymbol{P}_1^+$ along the [111] axis) together with the three possible propagation directions of the spin cycloid $\boldsymbol{k}_1 \| [\bar{1}10]$, $\boldsymbol{k}_2 \| [01\bar{1}]$ and $\boldsymbol{k}_3 \| [10\bar{1}]$. **d**, Striped pattern of ferroelectric domains in the (001)-oriented BFO thin film probed by piezoresponse force microscopy (PFM). The right panel sketches the two pristine variants of ferroelectric domains ($\boldsymbol{P}_3^-$ and $\boldsymbol{P}_4^-$) separated by 71° domain walls found in the boxed area. The sketches in **a**, **c** and **d** are in top view with a small tilt.

radio-frequency (RF) excitation enable measurement of the ESR spectrum of the NV defect by recording its spin-dependent photoluminescence intensity (Fig. 2b). Any magnetic field emanating from the sample is then detected through a Zeeman shift of the ESR frequency, which is simply given by $\Delta_z = \gamma_e B_{NV}/2\pi$, where $\gamma_e/2\pi = 28\,\mathrm{GHz\,T^{-1}}$ is the electronic spin gyromagnetic ratio and B_{NV} is the magnetic field projection along the NV defect quantization axis. The resulting magnetic sensitivity is in the range of a few $\mu\mathrm{T\,Hz}^{-1/2}$, while the spatial resolution is fixed by the distance d between the sample and the NV spin sensor[10]. This key parameter is independently measured through a calibration process above the edges of a uniformly magnetized ferromagnetic wire[24], leading to $d = 49.0 \pm 2.4\,\mathrm{nm}$ (Methods and Extended Data Fig. 4). In the following, all experiments are performed under ambient conditions with a bias field $B_b = 1.4\,\mathrm{mT}$ applied along the NV defect axis in order to determine the sign of the measured magnetic fields[10]. Such a bias field is weak enough not to modify the magnetic order in BFO.

The scanning-NV magnetometer was first operated in the dual-iso-B imaging mode by monitoring the signal $\mathcal{S} = \mathrm{PL}(\nu_2) - \mathrm{PL}(\nu_1)$, corresponding to the difference of photoluminescence (PL) intensity for two fixed RF frequencies, ν_1 and ν_2, applied consecutively at each point of the scan[10] (Fig. 2b). A typical dual-iso-B image recorded above the (001)-oriented BFO thin film is shown in Fig. 2c. We observe a periodic variation of the magnetometer signal along the horizontal axis in Fig. 2c, which directly reveals the spatially oscillating magnetic field generated by the cycloidal modulation of the spin order. Moreover, the propagation direction of this spin cycloid is periodically modified along the vertical axis in Fig. 2c. The resulting zig-zag shaped magnetic field distribution mimics the shape and width (about 100 nm) of ferroelectric domains (Fig. 1d).

To gain further insights into the properties of the spin cycloid in this BFO thin film, PFM was used to define a single micrometre-sized ferroelectric domain with $\boldsymbol{P}_1^+$ polarization within the as-grown striped pattern (Fig. 3a), taking advantage of the trailing electric field induced by the slow scan axis of the scanning probe (Methods). The magnetic field distribution recorded above such a ferroelectric monodomain exhibits a simple periodic structure, indicating the presence of a single spin cycloid (Fig. 3b). Importantly, the (001) surface projection of the spin cycloid propagation direction is normal to that of the ferroelectric polarization vector, $\boldsymbol{P}_1^+$. Among the three possible cycloid propagation directions, only $\boldsymbol{k}_1$ is normal to the (001) projection of $\boldsymbol{P}_1^+$; the other two lie at 45° from the polarization vector (Fig. 3c inset). We therefore conclude that the spin cycloid propagates along $\boldsymbol{k}_1$, that is, in the plane of the BFO thin film. This result can be qualitatively explained by considering that epitaxial strain modifies the anisotropy along the film normal[22]. For BFO thin films grown on $DyScO_3$, compressive strain induces an easy-plane contribution which stabilizes magnetic structures with their spins far from the [001] direction. Thus, the three possible cycloidal directions see their degeneracy lifted and the one propagating along $[\bar{1}10]$ becomes energetically favourable[22]. Using a two-dimensional fit of the magnetic image with a sinusoidal function, we infer a characteristic wavelength $\lambda = 70.6 \pm 1.4\,\mathrm{nm}$ (Fig. 3c). The slightly enhanced period compared to the bulk value (approximately 64 nm) is interpreted as being due to the small compressive strain imposed by the substrate[25]. This result illustrates that the local magnetoelectric interaction between neighbouring atoms at the origin of the spin cycloid does not require thick films of BFO, that is, with thicknesses well above its characteristic wavelength, as previously speculated[26].

After demonstrating that the polarization and the cycloid propagation are intimately linked, we describe how this cycloid propagation direction can be manipulated using the magnetoelectric coupling. To this end, we define another ferroelectric domain with an in-plane

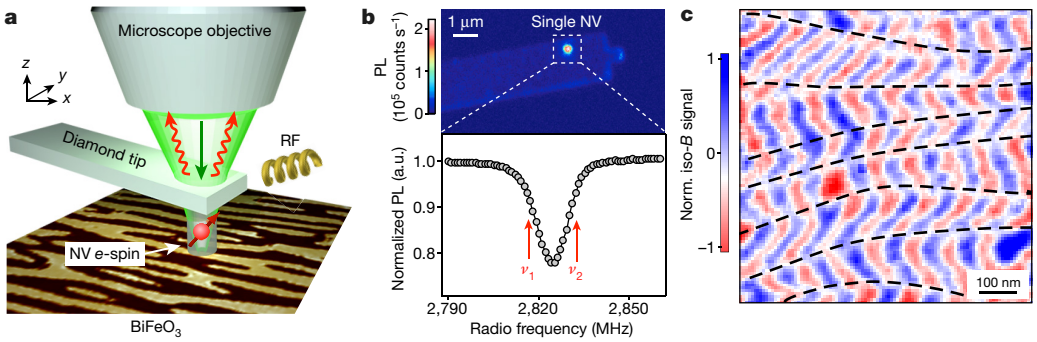

Figure 2 | Mapping the magnetic texture of BFO with NV magnetometry. a, The electronic spin of a single NV defect placed at the apex of a diamond scanning-probe tip is used as an atom-sized magnetic field sensor. A microscope objective enables both to excite (green arrow) and collect the spin-dependent photoluminescence (PL: red wavy arrows) of the NV defect, and a radiofrequency (RF) source is used to manipulate its electronic spin state (see Methods for details). **b**, Top panel, photoluminescence raster scan of the diamond scanning-probe showing the bright emission from a single NV defect; bottom panel, typical ESR spectrum recorded while applying a bias field $B_b = 1.4$ mT along the NV axis. The red arrows indicate the two RF frequencies ν_1 and ν_2 used for the dual-iso-B imaging mode (Methods). **c**, Magnetic field image recorded above the BFO film while operating the NV magnetometer in dual-iso-B imaging mode. The black dashed lines, which are drawn as guides to the eye, are attributed to ferroelectric domain walls leading to abrupt rotations of the cycloidal propagation vector.

component of the polarization rotated by 90° ($\boldsymbol{P}_4^-$ in Fig. 3d). The magnetic image shows that the propagation direction of the spin cycloid is also rotated by 90° with a very similar wavelength $\lambda = 71.4 \pm 1.4$ nm, once again corresponding to the propagation direction $\boldsymbol{k'}_1$ lying in the (001) plane (Fig. 3e, f). These experiments illustrate how magnetoelectric coupling can be used to efficiently control and manipulate the antiferromagnetic order in a BFO thin film. They also confirm that the abrupt rotations of the antiferromagnetic order observed in Fig. 2c are occurring at ferroelectric domain walls.

As a final experiment, a fully quantitative magnetic field image was recorded above the ferroelectric monodomain shown in Fig. 3a. Here the magnetic field component B_{NV} was obtained by measuring the Zeeman shift Δ_z of the NV defect electron spin sublevels at each pixel of the scan (Methods). The resulting magnetic field map indicates a modulation with a typical amplitude in the range of $\pm 140\,\mu$T (Fig. 4a). In order to understand quantitatively such experimental data, we start by computing the stray field produced by the BFO sample. The spin cycloid is modelled by a rotating uncompensated magnetization vector $\boldsymbol{M}_{eff} = \boldsymbol{m}_{eff}/V$, where V is the volume of the pseudo-cubic cell of BFO and

$$\boldsymbol{m}_{eff}(\boldsymbol{r'}) = m_{eff}[\cos(\boldsymbol{k}_1 \cdot \boldsymbol{r'})\boldsymbol{e}_{\boldsymbol{k}_1} + \sin(\boldsymbol{k}_1 \cdot \boldsymbol{r'})\boldsymbol{e}_P] \quad (1)$$

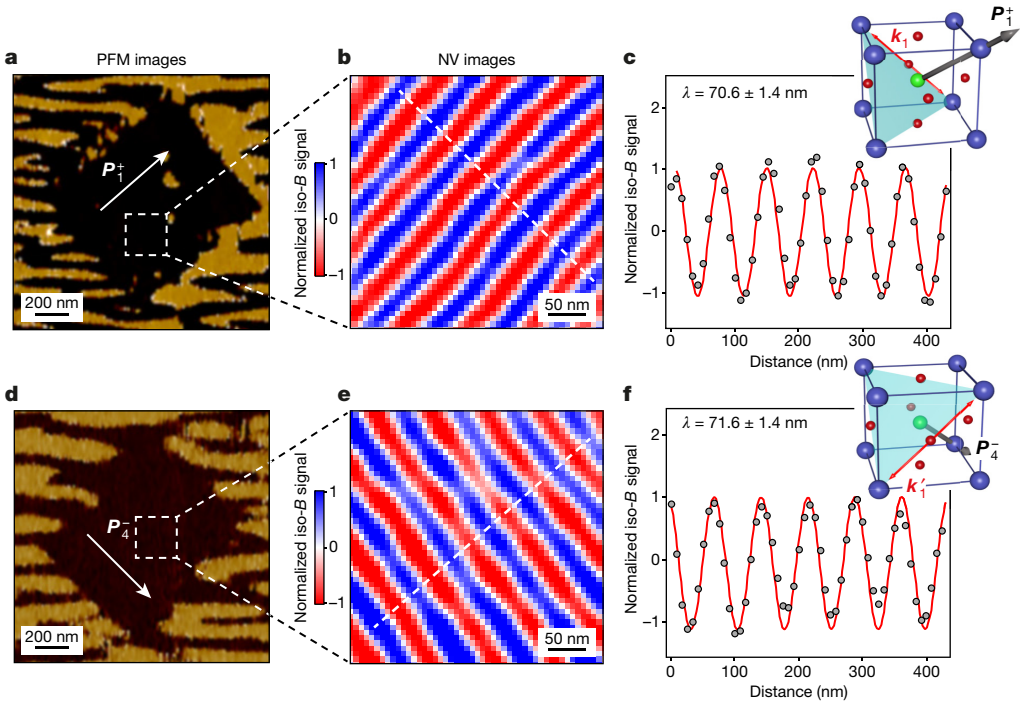

Figure 3 | Electrical control of the spin cycloid. a–**c**, For $\boldsymbol{P}_1^+$ polarization; **d**–**f**, for $\boldsymbol{P}_4^-$ polarization. **a**, **d**, In-plane PFM images of ferroelectric micrometre-sized domains with $\boldsymbol{P}_1^+$ and $\boldsymbol{P}_4^-$ polarizations, respectively. The white arrows indicate the in-plane projection of the ferroelectric polarization vector. **b**, **e**, Corresponding magnetic field distributions recorded from the respective boxed areas of **a** and **d** with the scanning-NV magnetometer operating in dual-iso-B imaging mode. **c**, **f**, Linecuts of the magnetic field distribution along the cycloid propagation direction (white dashed lines in **b** and **e**, respectively). The cycloid wavelength λ is extracted through a two-dimensional fit of the experimental data with a sinusoidal function (red solid lines). The standard error (s.e.) of the measurement (about 2%) is limited by the calibration of the scanner. Insets, top view sketches of the ferroelectric polarization vector together with the propagation vector of the spin cycloid $\boldsymbol{k}_1$ (in **c**) and $\boldsymbol{k'}_1$ (in **f**).

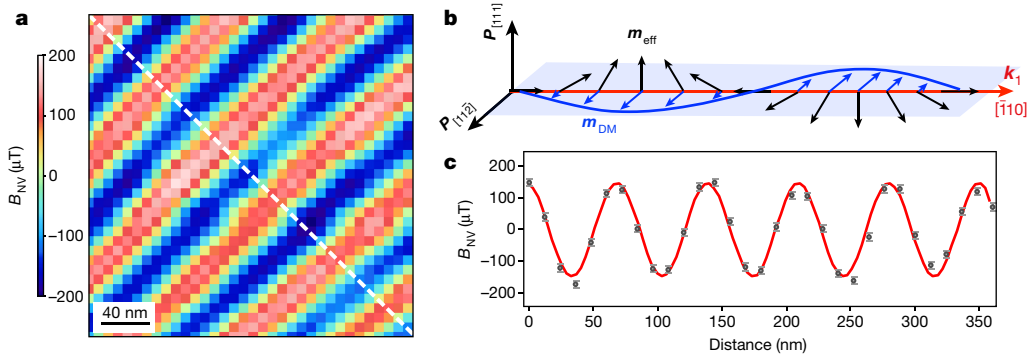

Figure 4 | Quantitative analysis of the spin cycloid magnetic texture. **a**, Fully quantitative magnetic field distribution B_{NV} recorded above the ferroelectric monodomain shown in Fig. 3a. **b**, Schematic representation of the spin density wave (SDW) corresponding to an uncompensated magnetic moment $\boldsymbol{m}_{DM}$ (blue arrows) oscillating in the $[11\bar{2}]$ direction, that is, perpendicular to both the ferroelectric polarization vector and $\boldsymbol{k}_1$. The uncompensated moment due to the pure cycloid $\boldsymbol{m}_{eff}$ is shown with black arrows. **c**, Linecut of the magnetic field distribution along the cycloid propagation direction (white dashed line in **a**). The black symbols are the experimental data with the standard error (s.e.) while the red solid line is the result of a fit using the analytical formula for the stray field produced by the BFO sample for $d = 49$ nm, $m_{eff} = 0.07\mu_B$, $\lambda = 70$ nm, $a = 0.396$ nm and $t = 32$ nm. The only free parameter is m_{DM}.

Here $||\boldsymbol{k}_1|| = 2\pi/\lambda$, $\boldsymbol{r}'$ denotes the coordinate in the BFO sample, while $\boldsymbol{e}_{\boldsymbol{k}_1}$ and $\boldsymbol{e}_{\boldsymbol{P}}$ are orthogonal unit vectors oriented along the cycloid propagation direction $\boldsymbol{k}_1$ and the ferroelectric polarization $\boldsymbol{P}$, respectively (Fig. 4b). The uncompensated magnetic moment per Fe atom is given by $m_{eff} = m_{Fe}\sin(\alpha_c/2)$, where $m_{Fe} = 4.1\mu_B$ is the measured magnetic moment of Fe atoms in BFO at room temperature[12] and α_c is the canting angle between antiferromagnetically coupled Fe atoms (Fig. 1b). This angle is directly deduced from the measured cycloid wavelength, leading to $\alpha_c = 2°$ and $m_{eff} = 0.07\mu_B$ (Methods).

The Dzyaloshinskii–Moriya (DM) interaction resulting from the alternate rotation of the FeO_6 octahedra along the [111] direction is another source of non-compensation of the magnetic moments in BFO[21,27]. In the homogeneous G-type state obtained at high magnetic fields (>20 T), this effect is known to generate a weak and uniform magnetization. In the cycloidal state, this magnetization is converted into a spin density wave (SDW) oscillating in the $[11\bar{2}]$ direction, which leads to a periodic wriggling of the cycloidal plane[28]. As sketched in Fig. 4b, the SDW can be simply modelled by an additional uncompensated magnetization vector $\boldsymbol{M}_{DM} = \boldsymbol{m}_{DM}/V$ such that:

$$\boldsymbol{m}_{DM}(\boldsymbol{r}') = m_{DM}\cos(\boldsymbol{k}_1 \cdot \boldsymbol{r}')(\boldsymbol{e}_{\boldsymbol{k}_1} \times \boldsymbol{e}_{\boldsymbol{P}}) \quad (2)$$

The value of the SDW amplitude m_{DM} remains a subject of debate. Although it is often considered to be small (about $0.03\mu_B$) or even negligible[21], polarized neutron scattering studies have revealed a maximum amplitude of $0.09\mu_B$ in bulk BFO[28], which is slightly larger than the uncompensated moment m_{eff} due to the pure cycloid.

An analytical calculation of the stray field produced above the BFO sample is given in Methods. We postulate here that the magnetic structure generating the stray field is a wriggling cycloid as described elsewhere[21,28]. The magnetic potential Φ produced by the magnetization pattern $\boldsymbol{M} = \boldsymbol{M}_{DM} + \boldsymbol{M}_{eff}$ is first calculated using Fourier methods for a monolayer of the BFO sample[29]. The resulting magnetic field is given by $\boldsymbol{B}^m = -\nabla\Phi$ and the total field $\boldsymbol{B}$ produced at a distance z above the BFO sample surface is finally obtained by summing the contribution from each monolayer. In the laboratory frame, (x, y, z) (Extended Data Fig. 5), the stray field components are given by

$$\begin{cases} B_x(\boldsymbol{r}) = -\mathcal{A}e^{-k_1 z}[C_1 m_{eff}\cos(\boldsymbol{k}_1 \cdot \boldsymbol{r}) - C_2 m_{DM}\sin(\boldsymbol{k}_1 \cdot \boldsymbol{r})] \\ B_y(\boldsymbol{r}) = \mathcal{A}e^{-k_1 z}[C_1 m_{eff}\cos(\boldsymbol{k}_1 \cdot \boldsymbol{r}) - C_2 m_{DM}\sin(\boldsymbol{k}_1 \cdot \boldsymbol{r})] \\ B_z(\boldsymbol{r}) = \sqrt{2}\,\mathcal{A}e^{-k_1 z}[C_1 m_{eff}\sin(\boldsymbol{k}_1 \cdot \boldsymbol{r}) + C_2 m_{DM}\cos(\boldsymbol{k}_1 \cdot \boldsymbol{r})] \end{cases} \quad (3)$$

where $C_1 = 1 + 1/\sqrt{3}$, $C_2 = 2/\sqrt{6}$, and

$$\mathcal{A} = \frac{\mu_0}{\sqrt{2}\,V}\left[\frac{1 - e^{-k_1 t}}{1 - e^{-k_1 a}}\right]\sinh\left(\frac{ak_1}{2}\right) \quad (4)$$

Here a is the thickness of a BFO monolayer and t the total thickness of the sample. These magnetic field components are then projected along the independently measured NV defect axis in order to obtain an analytical formula for B_{NV}. This formula was used to perform a two-dimensional fit of the experimental data while using m_{DM} as the only fitting parameter (Fig. 4c). A thorough analysis of uncertainties is given in Methods, including those related to (i) the fitting procedure itself, (ii) the probe-to-sample distance d, (iii) the cycloid wavelength λ, (iv) the sample thickness t and (v) the NV defect orientation. This analysis leads to $m_{DM} = (0.16 \pm 0.06)\mu_B$, where the overall uncertainty of about 40% mainly results from the imperfect knowledge of the probe-to-sample distance (Extended Data Fig. 6c). We note that the stray field produced above the BFO sample also depends on the chirality of the spin cycloid[29]. Equation (3) is obtained for a spin cycloid with an anticlockwise chirality. A similar analysis performed for a clockwise chirality would lead to a larger amplitude of the SDW, $m_{DM} = (0.21 \pm 0.08)\mu_B$ (Methods). In both cases, our study suggests a DM interaction much stronger than all reported values in the literature. This result could be explained by considering that the DM interaction is enhanced by the abrupt broken inversion symmetry occurring at the sample surface and then propagated in the BFO thin film by exchange interaction. This observation opens many perspectives for studying emergent interface-induced magnetic interactions resulting from a local breaking of inversion symmetry.

The present results show new ways to unravel intriguing phenomena occurring in multiferroic materials like BFO, ranging from magnetoelectric coupling[5] and peculiar properties induced by surface symmetry breaking, to conduction and magnetotransport properties at ferroelectric domain walls[19,30]. In a broader perspective, NV magnetometry appears to be a unique tool for studying the antiferromagnetic order at the nanoscale. In this way, similar investigations could be extended to a myriad of non-collinear antiferromagnetic materials, or to the domain walls of regular antiferromagnets, pointing the way towards the development of low-power spintronics[16].

Online Content Methods, along with any additional Extended Data display items and Source Data, are available in the online version of the paper; references unique to these sections appear only in the online paper.

Received 24 January; accepted 18 July 2017.

1. Coey, J. M. D. Noncollinear spin structures. *Can. J. Phys.* **65,** 1210–1232 (1987).
2. Kimura, T. *et al.* Magnetic control of ferroelectric polarization. *Nature* **426,** 55–58 (2003).
3. Cheong, S.-W. & Mostovoy, M. Multiferroics: a magnetic twist for ferroelectricity. *Nat. Mater.* **6,** 13–20 (2007).
4. Lottermoser, T. *et al.* Magnetic phase control by an electric field. *Nature* **430,** 541–544 (2004).
5. Heron, J. T. *et al.* Deterministic switching of ferromagnetism at room temperature using an electric field. *Nature* **516,** 370–373 (2014).
6. Nayak, A. K. *et al.* Large anomalous Hall effect driven by a nonvanishing Berry curvature in the noncolinear antiferromagnet Mn_3Ge. *Sci. Adv.* **2,** e1501870 (2016).
7. Zhang, W. *et al.* Giant facet-dependent spin-orbit torque and spin Hall conductivity in the triangular antiferromagnet $IrMn_3$. *Sci. Adv.* **2,** e1600759 (2016).
8. Maze, J. R. *et al.* Nanoscale magnetic sensing with an individual electronic spin in diamond. *Nature* **455,** 644–647 (2008).
9. Balasubramanian, G. *et al.* Nanoscale imaging magnetometry with diamond spins under ambient conditions. *Nature* **455,** 648–651 (2008).
10. Rondin, L. *et al.* Magnetometry with nitrogen-vacancy defects in diamond. *Rep. Prog. Phys.* **77,** 056503 (2014).
11. Sosnowska, I., Neumaier, T. P., Steichele, E., Peterlin-Neumaier, T. & Steichele, E. Spiral magnetic ordering in bismuth ferrite. *J. Phys. Chem.* **15,** 4835–4846 (1982).
12. Lebeugle, D. *et al.* Electric-field-induced spin flop in $BiFeO_3$ single crystals at room temperature. *Phys. Rev. Lett.* **100,** 227602 (2008).
13. Hartmann, U. Magnetic force microscopy. *Annu. Rev. Mater. Sci.* **29,** 53–87 (1999).
14. Locatelli, A. & Bauer, E. Recent advances in chemical and magnetic imaging of surfaces and interfaces by XPEEM. *J. Phys. Condens. Matter* **20,** 093002 (2008).
15. Wiesendanger, R. Spin mapping at the nanoscale and atomic scale. *Rev. Mod. Phys.* **81,** 1495–1550 (2009).
16. Jungwirth, T., Marti, X., Wadley, P. & Wunderlich, J. Antiferromagnetic spintronics. *Nature Nanotechnol.* **11,** 231–241 (2016).
17. Catalan, G. & Scott, J. F. Physics and applications of bismuth ferrite. *Adv. Mater.* **21,** 2463–2485 (2009).
18. Rovillain, P. *et al.* Electric-field control of spin waves at room temperature in multiferroic $BiFeO_3$. *Nat. Mater.* **9,** 975–979 (2010).
19. Balke, N. *et al.* Enhanced electric conductivity at ferroelectric vortex cores in $BiFeO_3$. *Nat. Phys.* **8,** 81–88 (2011).
20. Catalan, G., Seidel, J., Ramesh, R. & Scott, J. F. Domain wall nanoelectronics. *Rev. Mod. Phys.* **84,** 119–156 (2012).
21. Park, J.-G., Le, M. D., Jeong, J. & Lee, S. Structure and spin dynamics of multiferroic $BiFeO_3$. *J. Phys. Cond. Mat.* **26,** 433202 (2014).
22. Sando, D. *et al.* Crafting the magnonic and spintronic response of $BiFeO_3$ films by epitaxial strain. *Nat. Mater.* **12,** 641–646 (2013).
23. Maletinsky, P. *et al.* A robust scanning diamond sensor for nanoscale imaging with single nitrogen-vacancy centres. *Nature Nanotechnol.* **7,** 320–324 (2012).
24. Tetienne, J. P. *et al.* The nature of domain walls in ultrathin ferromagnets revealed by scanning nanomagnetometry. *Nat. Commun.* **6,** 6733 (2015).
25. Agbelele, A. *et al.* Strain and magnetic field induced spin-structure transitions in multiferroic $BiFeO_3$. *Adv. Mater.* **29,** 1602327 (2017).
26. Bertinshaw, J. *et al.* Direct evidence for the spin cycloid in strained nanoscale bismuth ferrite thin films. *Nat. Commun.* **7,** 12664 (2016).
27. Ederer, C. & Spaldin, N. A. Weak ferromagnetism and magnetoelectric coupling in bismuth ferrite. *Phys. Rev. B* **71,** 060401(R) (2005).
28. Ramazanoglu, M. *et al.* Local weak ferromagnetism in single-crystalline ferroelectric $BiFeO_3$. *Phys. Rev. Lett.* **107,** 207206 (2011).
29. Mikuszeit, N., Meckler, S., Wiesendanger, R. & Miranda, R. Magnetostatics and the rotational sense of cycloidal spin spirals. *Phys. Rev. B* **84,** 054404 (2011).
30. He, Q. *et al.* Magnetotransport at domain walls in $BiFeO_3$. *Phys. Rev. Lett.* **108,** 067203 (2012).

Acknowledgements We thank J. P. Tetienne and T. Hingant for experimental assistance in the early stages of the project. We are grateful to J. M. D. Coey for discussions. This research was supported by the European Research Council (ERC-StG-2014, IMAGINE), the European Union Seventh Framework Program (FP7/2007-2013) under the project DIADEMS, and by the French Agence Nationale de la Recherche (ANR) through project FERROMON and PIAF. This work is supported by a public grant overseen by the French National Research Agency (ANR) as part of the 'Investissements d'Avenir' program (Labex NanoSaclay, reference: ANR-10-LABX-0035).

Author Contributions I.G., W.A., L.J.M. and S.C. performed the NV magnetometry experiments; I.G., W.A., L.J.M. and V.J. analysed the data and performed magnetic modelling with assistance from M.V.; K.G. and C.C. fabricated the BFO sample; V.G. and S.F. performed the structural analysis and the piezoresponse force microscopy experiments; P.A. and P.M. engineered diamond tips hosting single NV defects; I.G., W.A., V.G., S.F., M.B. and V.J. wrote the manuscript. All authors contributed to the interpretation of the data and commented on the manuscript.

Author Information Reprints and permissions information is available at www.nature.com/reprints. The authors declare no competing financial interests. Readers are welcome to comment on the online version of the paper. Publisher's note: Springer Nature remains neutral with regard to jurisdictional claims in published maps and institutional affiliations. Correspondence and requests for materials should be addressed to V.J. (vincent.jacques@umontpellier.fr).

Reviewer Information *Nature* thanks J. Mundy and the other anonymous reviewer(s) for their contribution to the peer review of this work.

METHODS

Sample growth. The epitaxial thin film heterostructure was grown by pulsed laser deposition using a KrF excimer laser ($\lambda = 248$ nm, 1 J cm^{-2}) on an orthorhombic $DyScO_3$ $(110)_o$ single crystal substrate. The $SrRuO_3$ bottom electrode (1.2 nm) was grown with 5 Hz repetition rate at 650 °C under 0.2 mbar of oxygen. The $BiFeO_3$ film (32 nm) was subsequently grown at 650 °C under 0.36 mbar of oxygen with 1 Hz repetition rate. The sample was slowly cooled down under high oxygen pressure. The film surface exhibits single-unit-cell atomic steps (Extended Data Fig. 1a).

Structural properties. We investigated the structural properties of the $BiFeO_3$ thin film by X-ray diffraction (XRD). $DyScO_3$ has an orthorhombic structure[31] (*Pbnm*) with $a_o = 0.5440$ nm, $b_o = 0.5717$ nm and $c_o = 0.7903$ nm but can be described in a monoclinic cell on its $(110)_o$ orientation[32]. The two in-plane directions are then $\boldsymbol{a} \| [001]_o$ and $\boldsymbol{b} \| [\bar{1}10]_o$ and the out-of-plane $\boldsymbol{c}$ axis is slightly tilted so that $\alpha = 2\tan^{-1}\left(\frac{a_0}{b_0}\right) = 87.2°$, $\beta = \gamma = 90°$, $a = \frac{c_0}{2} = 0.3952$ nm, $b = c = \frac{\sqrt{a_0^2 + b_0^2}}{2} = 0.3947$ nm. In the following, we will only use the monoclinic notation for $DyScO_3$ and $BiFeO_3$.

The ω–2θ pattern shows only $(00l)$ peaks for $DyScO_3$ and $BiFeO_3$ indicating that the film is epitaxial and single phase (Extended Data Fig. 1b). In addition, the presence of Laue fringes indicates a well-crystallized structure and the peak-to-peak spacing corresponds to a thickness of 32 nm (Extended Data Fig. 1b).

To get more insights into the structure of $BiFeO_3$ thin films, we performed reciprocal space mappings (RSMs) along different directions of the monoclinic $DyScO_3$ substrate (Extended Data Fig. 2). The films are coherently strained as shown by the same $Q_{x,y}$ as the substrate for $(00l)_D$, $(h0l)_D$ and $(0kl)_D$ RSMs. Furthermore, two Q_z film variants are observed for $(h0l)_D$ RSMs and only one for $(0kl)_D$ RSMs. Thus, the RSM data are fully consistent with only two monoclinic domains of BFO epitaxially grown on top of $DyScO_3$ (ref. 33). For the first one, $(001)_B \| (001)_D$ and $[100]_B \| [110]_D$ (green colour in Extended Data Fig. 2), while the second one is rotated in plane by 90° so that $(001)_B \| (001)_D$ and $[100]_B \| [\bar{1}10]_D$ (blue colour in Extended Data Fig. 2). We found $\beta = 89.2°$, $\alpha = \gamma = 90°$, $a = 0.5601$ nm, $b = 0.5572$ nm and $c = 0.3991$ nm for the structural parameters of BFO thin films in the monoclinic cell representation. This corresponds to a pseudo-cubic unit-cell volume $V = 0.06227$ nm^3.

Ferroelectric properties. PFM experiments were conducted with an atomic force microscope (Nanoscope V multimode, Bruker) and two external SR830 lock-in detectors (Stanford Research) for simultaneous acquisition of in-plane and out-of-plane responses. A DS360 external source (Stanford Research) was used to apply the AC excitation to the $SrRuO_3$ bottom electrode at a frequency of 35 kHz while the conducting Pt coated tip was grounded. The hysteresis cycle of the out-of-plane PFM is shifted towards positive bias voltage values (Extended Data Fig. 3a), in accordance with the homogeneous pristine downward polarization detected by out-of-plane PFM imaging (Extended Data Fig. 3b).

The ferroelectric configuration of the pristine BFO sample was identified by vectorial PFM, that is, probing the different in-plane variants when rotating the sample crystallographic axis compared to the PFM cantilever long axis (Extended Data Fig. 3c–k)[34]. Alternating light/dark stripes are observed in the in-plane PFM phase image acquired with the cantilever aligned along the pseudocubic $[100]_c$ direction (Extended Data Fig. 3c or Fig. 1d). This configuration does not lift the degeneracy between equivalent polarization variants for PFM response: all four variants with polarization pointing downwards (sketched in Extended Data Fig. 3e) correspond to the same in plane amplitude response (Extended Data Fig. 3d). $\boldsymbol{P}_2^-$ and $\boldsymbol{P}_3^-$ are pointing to the right of the cantilever, corresponding to the dark phase signal, while $\boldsymbol{P}_1^-$ and $\boldsymbol{P}_4^-$ are pointing to the left of the cantilever, corresponding to the light phase signal. At this stage, several kinds of domain walls are still possible (for instance 109° domain walls between $\boldsymbol{P}_1^-$ and $\boldsymbol{P}_3^-$, or 71° domain walls between $\boldsymbol{P}_1^-$ and $\boldsymbol{P}_2^-$). When the cantilever is aligned along $[110]_c$ (Extended Data Fig. 3f), the $\boldsymbol{P}_2^-$ and $\boldsymbol{P}_4^-$ in-plane responses are turned off and all responding domains (bright amplitude in Extended Data Fig. 3g) are pointing to the left side of the cantilever (light phase signal in Extended Data Fig. 3h), identifying $\boldsymbol{P}_3^-$ domains. When the cantilever is aligned along $[\bar{1}10]_c$ (Extended Data Fig. 3i), the $\boldsymbol{P}_1^-$ and $\boldsymbol{P}_3^-$ in-plane responses are turned off and all responding domains (bright amplitude in Extended Data Fig. 3j) are pointing to the right of the cantilever (dark phase in Extended Data Fig. 3k), identifying $\boldsymbol{P}_4^-$ domains. Note that Extended Data Figs 3g and j show complementary responses, so that the ferroelectric configuration in BFO thin films that we present in the manuscript is determined as alternating $\boldsymbol{P}_3^-$ and $\boldsymbol{P}_4^-$ variants in the form of stripes separated by 71° domain walls.

In written areas (Fig. 3a, d), single ferroelectric domains are reproducibly obtained: the out-of-plane component of the polarization is controlled by the above coercive bias applied between the scanning tip and the bottom $SrRuO_3$ electrode. Moreover, the in-plane component is simultaneously defined thanks to the trailing field induced by the tip motion along the slow scan axis and aligned along the targeted polarization variant[35,36].

Scanning-NV magnetometry. The experimental set-up is described in detail in ref. 37. It combines a tuning-fork-based atomic force microscope (AFM) and a confocal optical microscope (attoAFM/CFM, Attocube Systems), all operating under ambient conditions. The NV spin sensor is located at the apex of a nanopillar in a diamond cantilever which is attached to the AFM head. The procedure for engineering the all-diamond scanning probe tips containing single NV defects used in this work can be found in ref. 38. Electron spin resonance (ESR) spectroscopy was performed by monitoring the NV defect photoluminescence (PL) intensity while sweeping the frequency of a RF field generated by a gold stripline antenna directly fabricated onto the BFO sample by e-beam lithography. The NV defect quantization axis was measured by recording the ESR frequency as a function of the amplitude and orientation of a calibrated magnetic field[39]. We obtain spherical angles ($\theta = 128° \pm 1°$, $\phi = 80° \pm 1°$) in the laboratory frame of reference (x, y, z).

Magnetic field images recorded in dual-iso-B imaging mode are obtained with an integration time of 200 ms per pixel. The quantitative magnetic field distribution shown in Fig. 4a is recorded by measuring the ESR spectrum at each pixel of the scan. This spectrum is composed of 10 bins with a bin size of 2 MHz and an integration time per bin of 65 ms, leading to a total acquisition time of 650 ms per spectrum. The magnetic field image shown in Fig. 4a is thus obtained within about 20 min. Each spectrum is fitted with a Gaussian function in order to infer the Zeeman shift of the ESR frequency, and thus the magnetic field B_{NV}. The intrinsic standard error (s.e.) of the magnetic field measurement is in the range of about 10 μT (see error bars in Fig. 4c).

Calibration of the probe-to-sample distance. The distance d between the NV spin sensor and the sample surface was inferred by recording the stray magnetic field produced above the edges of an uniformly magnetized ferromagnetic wire (Extended Data Fig. 4a). A typical Zeeman-shift profile recorded while scanning the NV defect across the edges of a 500-nm-wide wire of Pt/Co(0.6 nm)/AlO_x is shown in Extended Data Fig. 4b. The probe-to-sample distance d is then extracted by fitting the experimental data following the procedure described in refs 24, 40. The result of the fit is indicated as a red solid line in Extended Data Fig. 4b, showing a very good agreement with experimental data. The uncertainty and reproducibility of the fitting procedure was first inferred by fitting a set of independent measurements, leading to a relative uncertainty of 1.5% in probe-to-sample distance. Additional uncertainties induced by those on (i) the NV spin characteristics and (ii) the sample geometry were then carefully analysed following the method described in ref. 24, leading to $d = 49.0 \pm 2.4$ nm. The overall uncertainty is thus of the order of 5%.

Stray magnetic field produced by the spin cycloid. In this section, we calculate the stray magnetic field produced by the spin cycloid. The general methodology can be summarized as follows. The spin texture of the BFO sample is first modelled by a magnetization vector $\boldsymbol{M}$ describing a cycloid. The magnetic potential Φ produced by a single layer of the sample is then computed using Fourier methods and the resulting magnetic field $\boldsymbol{B}^m$ is obtained by using the relation $\boldsymbol{B}^m = -\nabla\Phi$. The total magnetic field $\boldsymbol{B}$ produced at a distance z above the sample is then calculated by summing up the contributions from all monolayers. The resulting magnetic field distribution is finally projected along the NV defect axis in order to obtain an analytical formula for B_{NV}, which can be used to fit the experimental data. The geometry used for the calculation is schematically depicted in Extended Data Fig. 5.

As introduced in the main text, we consider the uncompensated magnetic moments induced (i) by the pure spin cycloid $\boldsymbol{m}_{eff}$ and (ii) by the spin density wave $\boldsymbol{m}_{DM}$ (Fig. 4b). The resulting spin texture of the BFO sample is modelled by a magnetization vector $\boldsymbol{M} = (\boldsymbol{m}_{eff} + \boldsymbol{m}_{DM})/V$, where

$$\boldsymbol{m}_{eff}(\boldsymbol{r'}) = m_{eff}[\cos(\boldsymbol{k}_1 \cdot \boldsymbol{r'})\boldsymbol{e}_{\boldsymbol{k}_1} + \sin(\boldsymbol{k}_1 \cdot \boldsymbol{r'})\boldsymbol{e}_P] \tag{5}$$

$$\boldsymbol{m}_{DM}(\boldsymbol{r'}) = m_{DM}\cos(\boldsymbol{k}_1 \cdot \boldsymbol{r'})(\boldsymbol{e}_{\boldsymbol{k}_1} \times \boldsymbol{e}_P) \tag{6}$$

A rotation matrix was used to translate this magnetization into the laboratory frame of reference (x, y, z), in which the NV defect quantization axis is defined.

We start by computing the magnetic potential $\Phi(x, y, z)$ produced by a monolayer of the BFO sample, that is, with a unit cell thickness $a = 0.395$ nm. The magnetic potential is given by[29,41]:

$$\Phi(x,y,z) = \int_{x',y'=-\infty}^{x',y'=+\infty} \int_{z'=-a/2}^{z'=+a/2} -\frac{\mu_0}{4\pi}\boldsymbol{M}(x',y') \cdot \nabla\left(\frac{1}{\sqrt{(x-x')^2 + (y-y')^2 + (z-z')^2}}\right) \mathrm{d}x'\,\mathrm{d}y'\,\mathrm{d}z' \tag{7}$$

This equation includes a two-dimensional convolution defined as

$$f(x,y)*g(x,y)=\iint_{x',y'=-\infty}^{x',y'=+\infty} f(x',y')\,g(x-x',y-y')\,\mathrm{d}x'\,\mathrm{d}y' \tag{8}$$

so that the magnetic potential can be expressed as

$$\Phi(x,y,z)=-\frac{\mu_0}{4\pi}\int_{z'=-a/2}^{z'=+a/2}\left[\left(M_x*\frac{\partial}{\partial x}\frac{1}{r_0}\right)+\left(M_y*\frac{\partial}{\partial y}\frac{1}{r_0}\right)+\left(M_z*\frac{\partial}{\partial z}\frac{1}{r_0}\right)\right]\mathrm{d}z' \tag{9}$$

where

$$\frac{1}{r_0}=\frac{1}{\sqrt{x^2+y^2+(z-z')^2}} \tag{10}$$

and M_x, M_y, M_z are the components of the magnetization.

Taking the Fourier transform of equation (9) and using the convolution theorem $\mathcal{F}[f*g]=\mathcal{F}[f]\mathcal{F}[g]$, we obtain

$$\begin{aligned}\mathcal{F}(\Phi)=-\frac{\mu_0}{4\pi}\int_{z'=-a/2}^{z'=+a/2}\Bigg[&\mathcal{F}(M_x)\mathcal{F}\left(\frac{\partial}{\partial x}\frac{1}{r_0}\right)+\mathcal{F}(M_y)\mathcal{F}\left(\frac{\partial}{\partial y}\frac{1}{r_0}\right)\\&+\mathcal{F}(M_z)\mathcal{F}\left(\frac{\partial}{\partial z}\frac{1}{r_0}\right)\Bigg]\mathrm{d}z'\end{aligned} \tag{11}$$

Here M_x, M_y and M_z involve sine and cosine terms whose Fourier transforms are given by the Dirac δ function. The Fourier transform of the $\left(\frac{1}{r}\right)$ terms can be obtained by following the procedure described in ref. 41. The magnetic potential produced by a monolayer of the sample is finally obtained through an inverse Fourier transform leading to

$$\Phi(x,y,z)=\frac{\mu_0\sinh(ak_1/2)}{Vk_1}\mathrm{e}^{-k_1z}\{C_1m_{\mathrm{eff}}\sin(\boldsymbol{k}_1\cdot\boldsymbol{r})+C_2m_{\mathrm{DM}}\cos(\boldsymbol{k}_1\cdot\boldsymbol{r})\} \tag{12}$$

where $C_1=1+1/\sqrt{3}$ and $C_2=2/\sqrt{6}$.

The stray magnetic field $\boldsymbol{B}^m$ produced at a distance z above a monolayer was then calculated using the relation $\boldsymbol{B}^m=-\nabla\Phi$. The resulting stray field components are given by

$$\begin{cases}B_x^m=-\dfrac{\mu_0\sinh(ak_1/2)}{\sqrt{2}\,V}\mathrm{e}^{-k_1z}\{C_1\,m_{\mathrm{eff}}\cos(\boldsymbol{k}_1\cdot\boldsymbol{r})-C_2m_{\mathrm{DM}}\sin(\boldsymbol{k}_1\cdot\boldsymbol{r})\}\\ B_y^m=+\dfrac{\mu_0\sinh(ak_1/2)}{\sqrt{2}\,V}\mathrm{e}^{-k_1z}\{C_1\,m_{\mathrm{eff}}\cos(\boldsymbol{k}_1\cdot\boldsymbol{r})-C_2m_{\mathrm{DM}}\sin(\boldsymbol{k}_1\cdot\boldsymbol{r})\}\\ B_z^m=+\dfrac{\mu_0\sinh(ak_1/2)}{V}\mathrm{e}^{-k_1z}\{C_1\,m_{\mathrm{eff}}\sin(\boldsymbol{k}_1\cdot\boldsymbol{r})+C_2m_{\mathrm{DM}}\cos(\boldsymbol{k}_1\cdot\boldsymbol{r})\}\end{cases} \tag{13}$$

The total magnetic field $\boldsymbol{B}$ produced by the sample is obtained by summing the contribution of each monolayer

$$\begin{cases}B_x=\sum_{j=0}^{N-1}-\dfrac{\mu_0\sinh(ak_1/2)}{\sqrt{2}\,V}\mathrm{e}^{-k_1(z+ja)}\{C_1\,m_{\mathrm{eff}}\cos(\boldsymbol{k}_1\cdot\boldsymbol{r})-C_2\,m_{\mathrm{DM}}\sin(\boldsymbol{k}_1\cdot\boldsymbol{r})\}\\ B_y=\sum_{j=0}^{N-1}+\dfrac{\mu_0\sinh(ak_1/2)}{\sqrt{2}\,V}\mathrm{e}^{-k_1(z+ja)}\{C_1\,m_{\mathrm{eff}}\cos(\boldsymbol{k}_1\cdot\boldsymbol{r})-C_2\,m_{\mathrm{DM}}\sin(\boldsymbol{k}_1\cdot\boldsymbol{r})\}\\ B_z=\sum_{j=0}^{N-1}+\dfrac{\mu_0\sinh(ak_1/2)}{V}\mathrm{e}^{-k_1(z+ja)}\{C_1\,m_{\mathrm{eff}}\sin(\boldsymbol{k}_1\cdot\boldsymbol{r})+C_2\,m_{\mathrm{DM}}\cos(\boldsymbol{k}_1\cdot\boldsymbol{r})\}\end{cases} \tag{14}$$

where N is the number of atomic layer of the BFO sample.

The above equation can be further simplified as

$$\begin{cases}B_x=-\mathcal{A}\mathrm{e}^{-k_1z}\{C_1\,m_{\mathrm{eff}}\cos(\boldsymbol{k}_1\cdot\boldsymbol{r})-C_2\,m_{\mathrm{DM}}\sin(\boldsymbol{k}_1\cdot\boldsymbol{r})\}\\ B_y=+\mathcal{A}\mathrm{e}^{-k_1z}\{C_1\,m_{\mathrm{eff}}\cos(\boldsymbol{k}_1\cdot\boldsymbol{r})-C_2\,m_{\mathrm{DM}}\sin(\boldsymbol{k}_1\cdot\boldsymbol{r})\}\\ B_z=+\sqrt{2}\mathcal{A}\mathrm{e}^{-k_1z}\{C_1\,m_{\mathrm{eff}}\sin(\boldsymbol{k}_1\cdot\boldsymbol{r})+C_2\,m_{\mathrm{DM}}\cos(\boldsymbol{k}_1\cdot\boldsymbol{r})\}\end{cases} \tag{15}$$

where

$$\mathcal{A}=\frac{\mu_0}{\sqrt{2}\,V}\left[\frac{1-\mathrm{e}^{-k_1t}}{1-\mathrm{e}^{-k_1a}}\right]\sinh\left(\frac{ak_1}{2}\right) \tag{16}$$

Here $t=Na$ is the total thickness of the BFO sample.

This magnetic field distribution is finally projected along the NV defect axis in order to obtain an analytical formula for B_{NV}, which is given by

$$B_{\mathrm{NV}}=B_x\cos\phi\sin\theta+B_y\sin\phi\sin\theta+B_z\cos\theta \tag{17}$$

where (θ,ϕ) are the spherical angles of the NV axis in the laboratory frame. Equation (17) was used to perform a two-dimensional fit of the experimental data, while using m_{DM} as the only free parameter. The quality of the fit is illustrated by Extended Data Fig. 6b.

Analysis of uncertainties. We now analyse the uncertainty on the fit outcome m_{DM}, which results (i) from the fitting procedure and (ii) from uncertainties on the parameters $p_i=\{\lambda, m_{\mathrm{eff}}, t, d, \theta, \phi\}$ that are involved in the expression for B_{NV}. In the following, the parameters p_i are expressed as $p_i=\overline{p}_i+\sigma_{p_i}$ where $\overline{p}_i$ denotes the nominal value of parameter p_i and σ_{p_i} its standard error. These parameters, which are summarized in Extended Data Fig. 6c, are evaluated as follows:

•The cycloid wavelength λ can be precisely extracted through an independent two-dimensional fit of the experimental data with a simple sinusoidal function. We obtain $\lambda=70.0\pm1.4$ nm for the quantitative magnetic field image shown in Fig. 4. The uncertainty (about 2%) comes from the calibration of the (x, y) scanner.

•From the measured cycloid wavelength, we infer a characteristic canting angle of $\frac{360^\circ}{\lambda}=5.14^\circ\pm0.10^\circ/\mathrm{nm}$, leading to $\alpha_c=2.04\pm0.02^\circ$ between neighbouring antiferromagnetically coupled Fe atoms, which are separated by $a=0.395$ nm (see Fig. 1b). The resulting uncompensated magnetic moment per Fe atom is given by: $m_{\mathrm{eff}}=m_{\mathrm{Fe}}\sin(\alpha_c/2)=0.073\pm0.001\ \mu_{\mathrm{B}}$.

•The thickness of the BFO sample is extracted through X-ray diffraction (XRD) measurements (see Extended Data Fig. 1b). The peak-to-peak spacing of Laue fringes indicates a sample thickness $t=32\pm2$ nm.

•The NV defect quantization axis is measured by recording the ESR frequency as a function of the amplitude and orientation of a calibrated magnetic field, leading to spherical angles ($\theta=128\pm1^\circ$, $\phi=80\pm1^\circ$) in the laboratory frame (x, y, z).

•The probe-to-sample distance d is inferred through a calibration measurement described in the previous section, leading to $d=49.0\pm2.4$ nm.

We first evaluate the uncertainty of the fitting procedure. To this end, a two-dimensional fit of the experimental data was performed with equation (17) while fixing all the parameters p_i to their nominal values $\overline{p}_i$, leading to $m_{\mathrm{DM}}=0.160\pm0.002\,\mu_{\mathrm{B}}$. The relative uncertainty linked to the fitting procedure is therefore given by $\epsilon_{\mathrm{fit}}=1.2\%$. We note that the intrinsic accuracy of the magnetic field measurement is in the range of $\delta B_{\mathrm{NV}}\approx10\,\mu$T. This leads to an uncertainty of the SDW amplitude $\delta m_{\mathrm{DM}}\approx0.01\,\mu_{\mathrm{B}}$, corresponding to a relative uncertainty $\epsilon_{\mathrm{m}}=6\%$.

In order to estimate the relative uncertainty ϵ_{p_i} introduced by each parameter p_i, the two-dimensional fit was performed with one parameter p_i fixed at $p_i=\overline{p}_i\pm\sigma_{p_i}$, all the other five parameters remaining fixed at their nominal values. The corresponding fit outcomes are denoted $m_{\mathrm{DM}}(\overline{p}_i+\sigma_{p_i})$ and $m_{\mathrm{DM}}(\overline{p}_i-\sigma_{p_i})$. The relative uncertainty introduced by the errors on parameter p_i is then finally defined as:

$$\epsilon_{p_i}=\frac{m_{\mathrm{DM}}(\overline{p}_i+\sigma_{p_i})-m_{\mathrm{DM}}(\overline{p}_i-\sigma_{p_i})}{2m_{\mathrm{DM}}(\overline{p}_i)} \tag{18}$$

This analysis was performed for each parameter p_i and the resulting uncertainties ϵ_{p_i} are summarized in Extended Data Fig. 6c. The cumulative uncertainty ϵ is finally given by

$$\epsilon=\sqrt{\epsilon_{\mathrm{fit}}^2+\epsilon_{\mathrm{m}}^2+\sum_i\epsilon_{p_i}^2} \tag{19}$$

where all errors are assumed to be independent.

We finally obtain $\epsilon=41\%$ and $m_{\mathrm{DM}}=0.16\pm0.06\,\mu_{\mathrm{B}}$. We note that the dominant source of uncertainty is given by the imperfect knowledge of the probe-to-sample distance ($\epsilon_d=39\%$).

Comparison with numerical simulations. The only assumption used for the calculation of the stray field above the BFO sample consists of considering a two-dimensional spin texture with infinite size in the (x', y') plane (see Extended Data Fig. 5). Such an assumption is valid since the typical dimension of the ferroelectric monodomain is in the range of 1 μm, which is much larger than the probe-to-sample distance d. This was further verified by comparing the result of the calculation with numerical simulations. To this end, the magnetization $\boldsymbol{M}$ of the BFO sample was discretized into uniformly magnetized computation cells with a characteristic mesh volume 1 nm × 1 nm × 1 nm. The magnetic field distribution produced by each magnetization cell was computed at a distance d above the sample surface using standard magnetostatic theory[37]. By summing the contributions of all cells and then projecting along the NV defect quantization axis, we finally obtain

a simulation of the stray field distribution B_{NV}. Such a numerical simulation is in excellent agreement with the analytical calculation with a deviation smaller than 1%.

Effect of the cycloid chirality. In the previous sections, the calculation of the stray field above the BFO sample was performed for a spin cycloid with an anticlockwise (acw) chirality. It was emphasized in ref. 29 that the stray field depends on the chirality of the spin cycloid. By considering a clockwise (cw) chirality, the uncompensated magnetic moment induced by the spin cycloid is modified as

$$\boldsymbol{m}_{\text{eff}}^{(\text{cw})}(\boldsymbol{r'}) = m_{\text{eff}}[\cos(\boldsymbol{k}_1 \cdot \boldsymbol{r'})\mathbf{e}_{\mathbf{k_1}} - \sin(\boldsymbol{k}_1 \cdot \boldsymbol{r'})\boldsymbol{e_P}] \tag{20}$$

On the other hand, the magnetization distribution resulting from the SDW is independent of the chirality. The resulting magnetic field distribution is then given by

$$\begin{cases} B_x = -\mathcal{A}\mathrm{e}^{-k_1 z}\{C_1^{(\text{cw})} m_{\text{eff}} \cos(\boldsymbol{k}_1 \cdot \boldsymbol{r}) - C_2 m_{\text{DM}} \sin(\boldsymbol{k}_1 \cdot \boldsymbol{r})\} \\ B_y = +\mathcal{A}\mathrm{e}^{-k_1 z}\{C_1^{(\text{cw})} m_{\text{eff}} \cos(\boldsymbol{k}_1 \cdot \boldsymbol{r}) - C_2\, m_{\text{DM}} \sin(\boldsymbol{k}_1 \cdot \boldsymbol{r})\} \\ B_z = +\sqrt{2}\,\mathcal{A}\mathrm{e}^{-k_1 z}\{C_1^{(\text{cw})} m_{\text{eff}} \sin(\boldsymbol{k}_1 \cdot \boldsymbol{r}) + C_2\, m_{\text{DM}} \cos(\boldsymbol{k}_1 \cdot \boldsymbol{r})\} \end{cases} \tag{21}$$

where $C_1^{(\text{cw})} = 1 - 1/\sqrt{3}$. The only difference between this magnetic field distribution and the one obtained for an anticlockwise chirality is the constant $C_1^{(\text{cw})}$ (see equation (15)). Since $C_1^{(\text{cw})} < C_1$, the stray magnetic field produced by the pure cycloid is weaker for the clockwise chirality. Fitting the experimental data with such a chirality of the spin cycloid leads to $m_{\text{DM}} = 0.21 \pm 0.08\,\mu_{\text{B}}$. The cycloid chirality could be measured in future experiments by analysing the stray field amplitude on each side of a single ferroelectric domain wall. In this work, postulating either chirality leads to the similar conclusion that the DM interaction is much stronger than all reported values in the literature.

Data availability. The data that support the findings of this study are available from the corresponding author upon reasonable request.

31. Uecker, R. *et al.* Properties of rare-earth scandate single crystals (Re=Nd-Dy). *J. Cryst. Growth* **310,** 2649–2658 (2008).
32. Johann, F., Morelli, A., Biggemann, D., Arredondo, M. & Vrejoiu, I. Epitaxial strain and electric boundary condition effects on the structural and ferroelectric properties of $BiFeO_3$ films. *Phys. Rev. B* **84,** 094105 (2011).
33. Chen, Z. H., Damodaran, A. R., Xu, R., Lee, S. & Martin, L. W. Effect of symmetry mismatch on the domain structure of rhombohedral $BiFeO_3$ thin films. *Appl. Phys. Lett.* **104,** 182908 (2014).
34. Zavaliche, F. *et al.* Multiferroic $BiFeO_3$ films: domain structure and polarization dynamics. *Phase Transitions* **79,** 991–1017 (2006).
35. Balke, N. *et al.* Deterministic control of ferroelastic switching in multiferroic materials. *Nat. Nanotechnol.* **4,** 868–875 (2009).
36. Crassous, A., Sluka, T., Tagantsev, A. K. & Setter, N. Polarization charge as a reconfigurable quasi-dopant in ferroelectric thin films. *Nat. Nanotechnol.* **10,** 614–618 (2015).
37. Rondin, L. *et al.* Nanoscale magnetic field mapping with a single spin scanning probe magnetometer. *Appl. Phys. Lett.* **100,** 153118 (2012).
38. Appel, P. *et al.* Fabrication of all diamond scanning probes for nanoscale magnetometry. *Rev. Sci. Instrum.* **87,** 063703 (2016).
39. Rondin, L. *et al.* Stray-field imaging of magnetic vortices with a single diamond spin. *Nat. Commun.* **4,** 2279 (2013).
40. Hingant, T. *et al.* Measuring the magnetic moment density in patterned ultrathin ferromagnets with submicrometer resolution. *Phys. Rev. Appl.* **4,** 014003 (2015).
41. Blakely, R. J. *Potential Theory in Gravity and Magnetic Applications* (Cambridge Univ. Press, 1996).

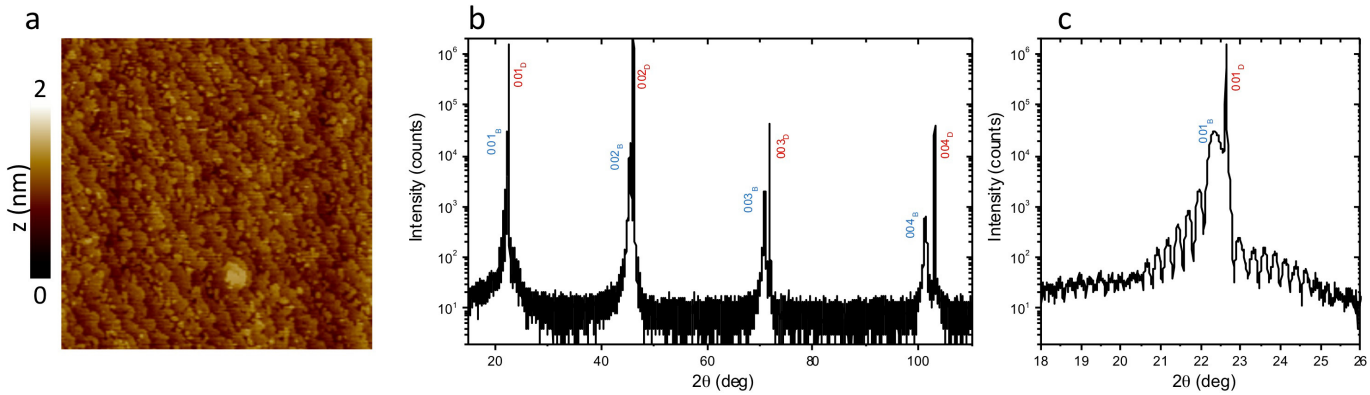

Extended Data Figure 1 | Structural properties of the magnetic thin film. a, The surface topography of the 6 μm × 6 μm 32-nm-thick $BiFeO_3$ (BFO) thin film grown on a $DyScO_3$ substrate, showing single-unit-cell atomic steps. **b**, X-ray diffraction ω–2θ pattern of the same film displays only (00*l*) peaks for BFO and $DyScO_3$ (in monoclinic notation). D (in red colour) and B (in blue colour) subscripts stand for $DyScO_3$ and $BiFeO_3$, respectively. **c**, Zoom along the (001) peak of $DyScO_3$, showing clear Laue fringes.

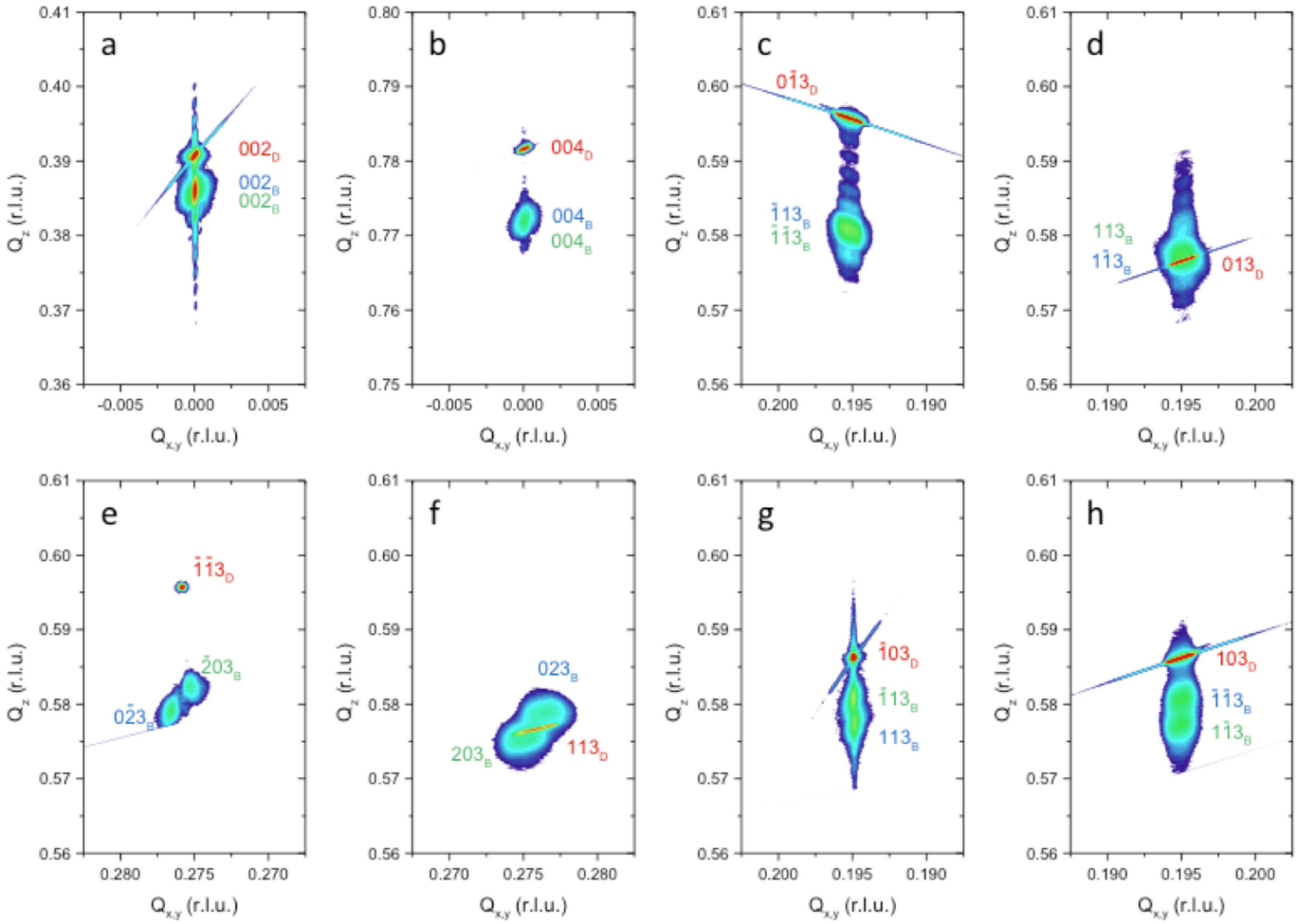

Extended Data Figure 2 | Reciprocal space mappings (RSMs) of the 32-nm-thick BFO film grown on $SrRuO_3/DyScO_3$. Shown are RSMs around **a**, $(002)_D$, **b**, $(004)_D$, **c**, $(0\bar{1}3)_D$, **d**, $(013)_D$, **e**, $(\bar{1}\bar{1}3)_D$, **f**, $(113)_D$, **g**, $(1\bar{0}3)_D$ and **h**, $(103)_D$ planes of $DyScO_3$. All the planes are indexed in monoclinic notation and the subscripts D and B correspond to $DyScO_3$ and BFO, respectively. Two different domains can be identified for monoclinic BFO (green and blue). $Q_{x,y}$ and Q_z indicate the in-plane and out-of-plane reciprocal space units, respectively.

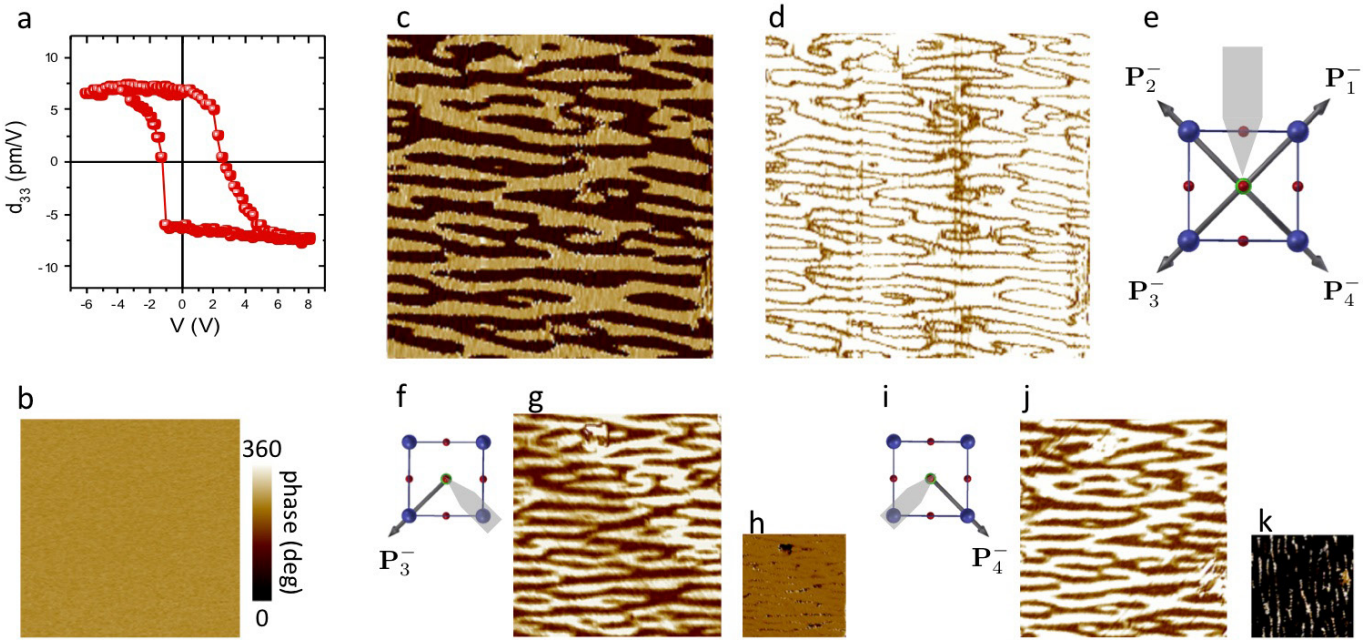

Extended Data Figure 3 | Determination of polarization variants in BFO thin films. a, Local out-of-plane PFM hysteresis loop with bias voltage. d_{33} is the out-of-plane piezoelectric coefficient. **b**, Homogeneous out-of-plane PFM phase corresponding to polarization variants pointing downward in a 6 μm × 6 μm area. **c**, In-plane PFM phase and **d**, amplitude for the cantilever parallel to $[100]_c$. **e**, Sketch of the PFM cantilever and the four possible in-plane variants of polarization in BFO. **f**, Sketch of the $[110]_c$ direction of the cantilever, with the corresponding in-plane PFM amplitude (**g**) and phase (**h**). **i**, Sketch of the $[\bar{1}10]_c$ direction of the cantilever with the corresponding in-plane PFM amplitude (**j**) and phase (**k**). All the images in **c** to **k** have been acquired in the same 3 μm × 3 μm area.

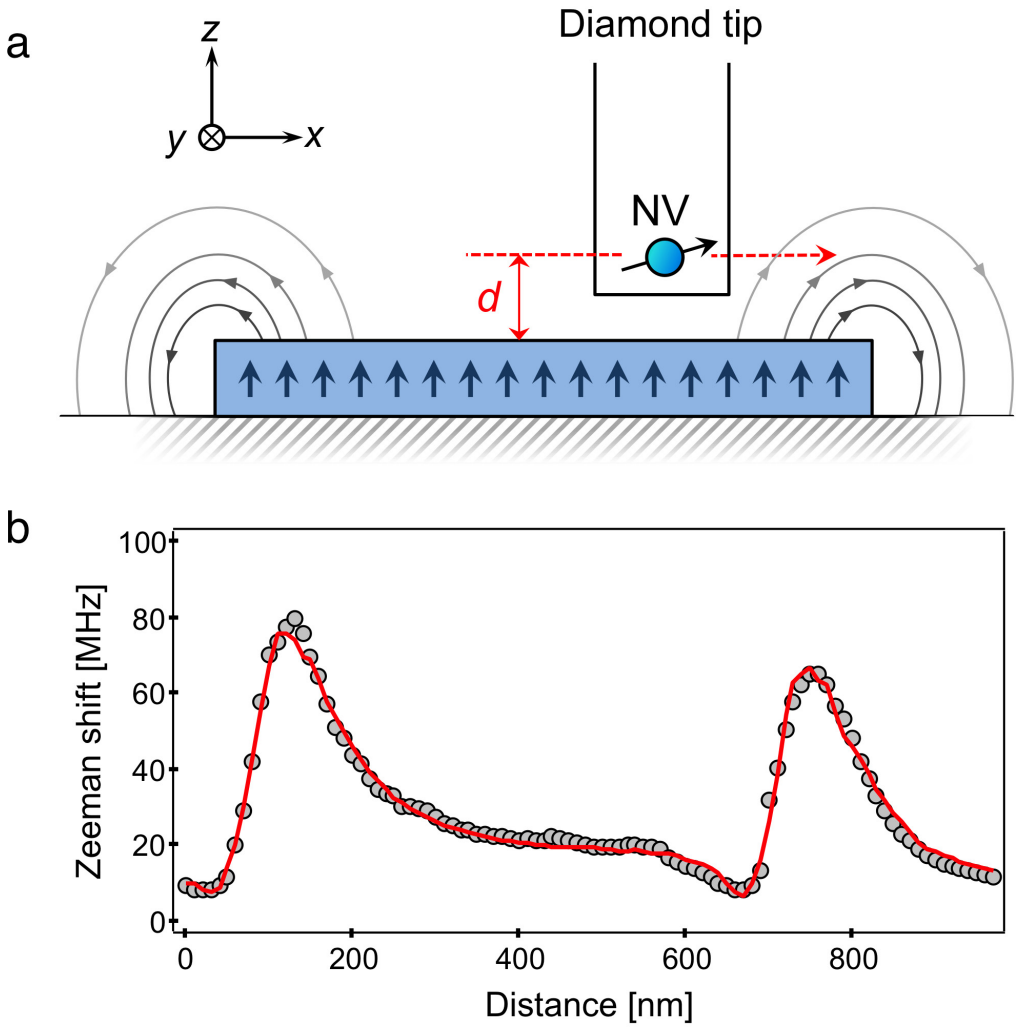

Extended Data Figure 4 | Measurement of the probe-to-sample distance. a, The scanning-NV magnetometer ('diamond tip') is used to measure the magnetic field (grey arrows) produced at the edges of an uniformly magnetized ferromagnetic wire (blue arrows). **b**, Typical Zeeman-shift profile measured by scanning the NV defect across the edges of a 500-nm-wide wire of Pt/Co(0.6nm)/AlO_x with perpendicular magnetic anisotropy. The circles are experimental data and the red solid line is data fitting from which distance d is extracted[24,40]. We note that only the absolute value of the magnetic field is measured in this experiment.

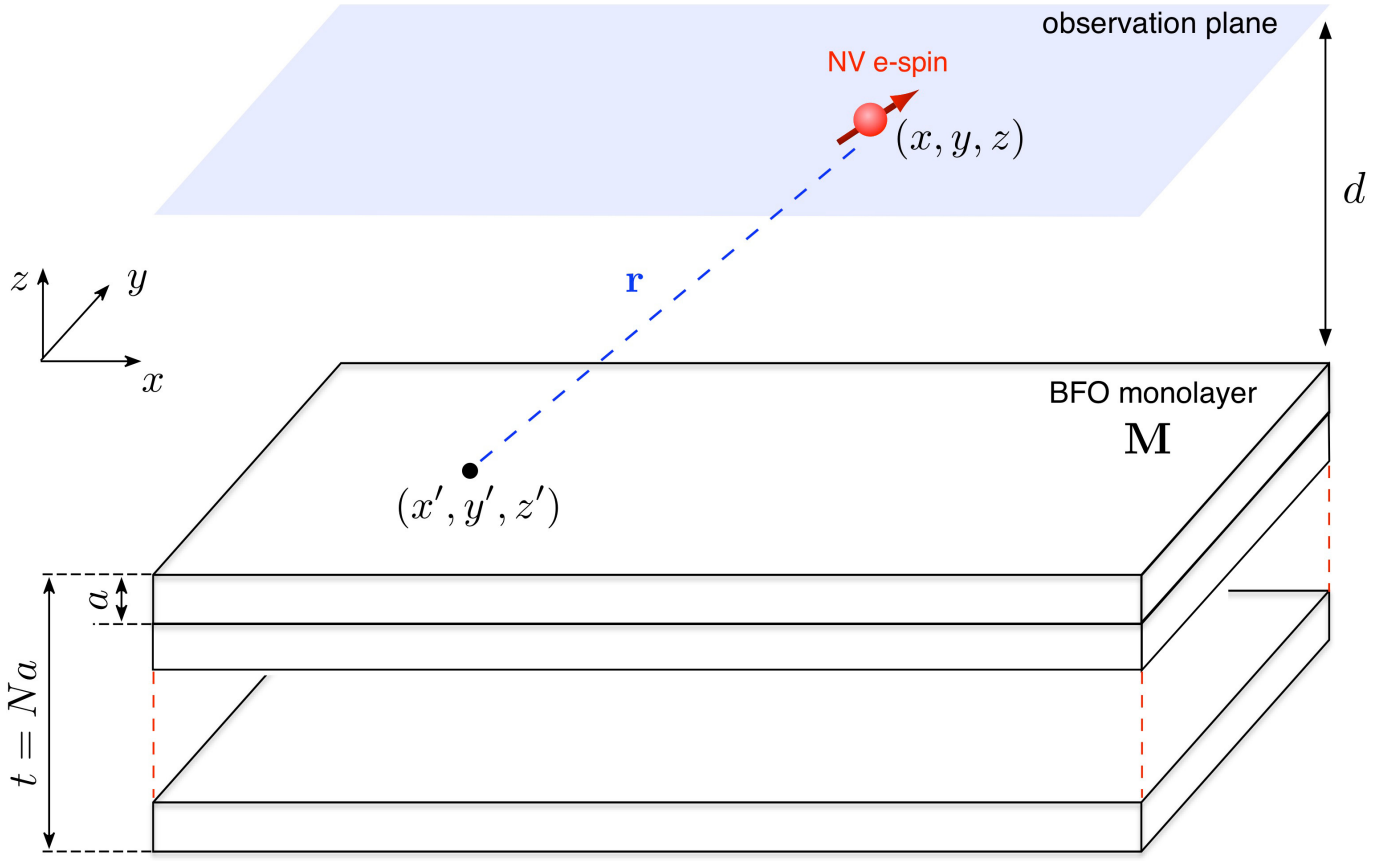

Extended Data Figure 5 | Schematic of the geometry used for the stray field calculation. The thickness, t, of the film is divided into N monolayers of thickness a. The blue plane represents the observation plane at a distance d from the BFO film. (x, y, z) and (x', y', z') represent, respectively, the coordinates of the observation point and the magnetic moment with respect to the laboratory frame. The red dashed lines indicate the remaining monolayers in the film that are not illustrated.

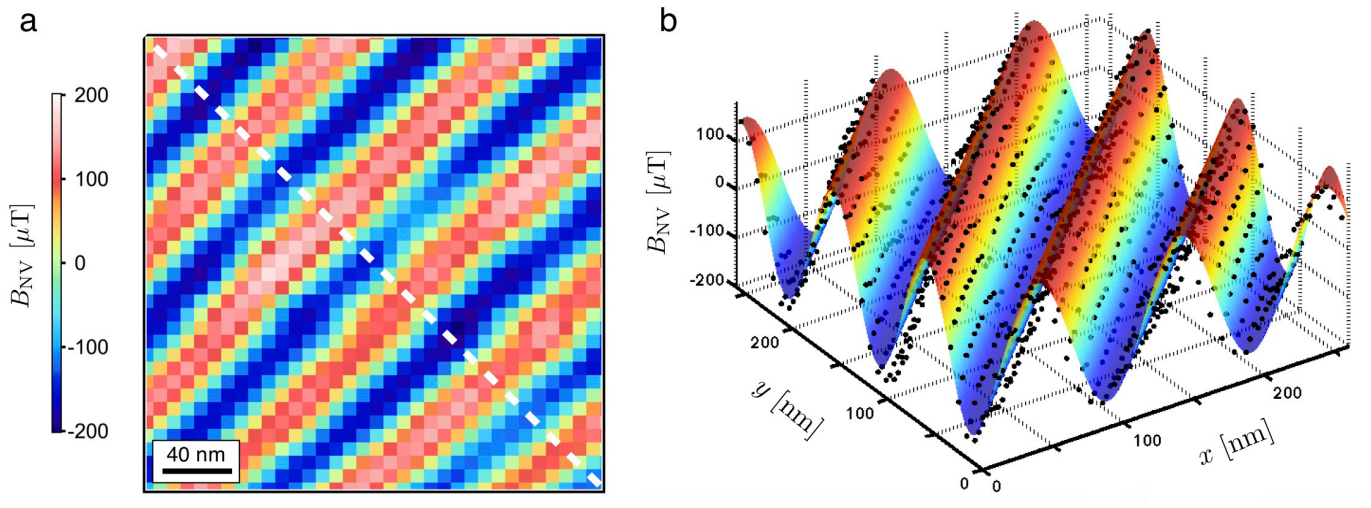

c

parameter p_i	nominal value $\bar{p}_i$	uncertainty σ_{p_i}	ϵ_{p_i}(%)
λ	70.0 nm	1.4 nm	12
m_{eff}	0.073 μ_B	0.001 μ_B	< 1
t	32 nm	2 nm	1
θ	128°	1°	1.5
ϕ	80°	1°	1.5
d	49 nm	2.4 nm	39

Extended Data Figure 6 | Data fitting and uncertainty analysis. **a**, Magnetic field distribution reproduced from Fig. 4a of the main text. **b**, The black symbols are the experimental data and the coloured solid curve is the result of a two-dimensional fit using equation (17) with $d = 49$ nm, $m_{\text{eff}} = 0.07\mu_B$, $\lambda = 70$ nm, $a = 0.396$ nm, $t = 32$ nm and $(\theta, \phi) = (128°, 80°)$. The linecut shown in Fig. 4c of the main text corresponds to the white dashed line in **a**. **c**, Summary of the relative uncertainties ϵ_{p_i} on the fitting parameter m_{DM} for the six parameters $p_i = \{\lambda, m_{\text{eff}}, t, d, \theta, \phi\}$ (see Methods for details).